

# Nonadditive Penetrable Mixtures in Nanopores: Surface-Induced Population Inversion

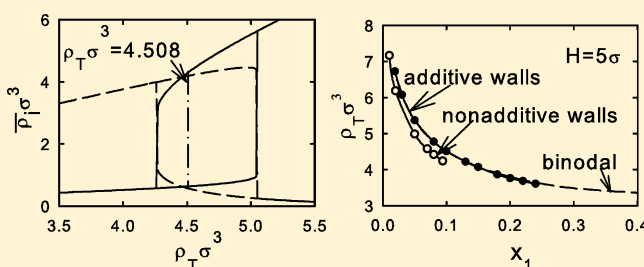
Eun-Young Kim<sup>†</sup> and Soon-Chul Kim\*

Department of Physics, Andong National University, Andong 760-749, Korea

Baek-Seok Seong

HANARO Center, Korea Advanced Energy Research Institute, Daejeon 305-600, Korea

**ABSTRACT:** We investigate the surface-induced population inversion of the nonadditive penetrable mixtures which exhibits the fluid–fluid demixing transition of the bulk system due to the confinement effect. The result shows that the population inversions are strongly affected by the extra repulsion between unlike species, the mole fraction of species, the width of nanopores, and the nonadditive walls. The extra repulsion between unlike species in a confined system increases the contact density of both species at the wall and promotes the population inversion in nanopores. The population inversion is the typical shift first-order fluid–fluid demixing transition due to the confinement effect in nanopores. The population inversions are only observed in nanopores with finite widths. The population inversion line is shifted toward a higher fluid density with decreasing width of the nanopores and lies slightly in lower density compared with the coexistence curves of the bulk system. The nonadditive wall for the big particles leads to the population inversion in lower density compared with that of the nonadditive wall for the small particles. The population inversion line is terminated at a lower mole fraction.



## 1. INTRODUCTION

The structure and phase behavior of a confined fluid mixture inside nanopores are known to be significantly different from the properties of the bulk fluid.<sup>1</sup> The equilibrium properties of the confined additive fluid mixtures are in part affected by the geometry of the pores and the fluid–pore interaction, while the equilibrium properties of nonadditive fluid mixtures that exhibit the fluid–fluid demixing transition in the bulk system are extremely sensitive to the extra repulsion between unlike species.<sup>2–15</sup> An understanding of the nonadditive fluid properties due to the size ratio of the components and confinement effects is of great interest not only for basic research but also for a broad variety of technological applications: one is the interfacial and wetting behaviors of the fluid mixtures, which is related to the first-order layering and critical prewetting transition near the slit wall.<sup>5–10</sup> The other is the population inversion of the nonadditive fluid mixtures in nanopores.<sup>11–17</sup>

Unlike the interfacial and wetting properties in nonadditive fluid mixtures, the population inversion of the nonadditive fluid mixtures in nanopores was recently studied by a few authors: Jiménez-Ángeles et al.<sup>11</sup> reported the surface-induced population inversion for the nonadditivity hard-sphere mixtures confined in cylindrical pores through the integral equation and computer simulations. They found that at lower or intermediate values of the total bulk density the denser bulk species was preferentially adsorbed in slit-like nanopores. Further increases

in the bulk density led to an abrupt population inversion in cylindrical pores. Kim et al.<sup>12</sup> also observed this population for the nonadditive hard-sphere mixtures in slit-like nanopores. Jiménez-Ángeles et al. and Kim et al. have shown that the population inversion line for nonadditive hard spheres is close to the bulk fluid coexistence line, but the two phenomena are different. Afterward, Ayadim and Amokrane<sup>13</sup> have shown that accurate integral equations can predict the population inversion threshold for nonadditive hard spheres in a slit-like pore. Brunet et al.<sup>15</sup> discussed the population inversion and effect of an external field on nonadditive mixtures on the basis of Monte Carlo simulations. More recently, Taghizadeh and Keshavarzi<sup>16</sup> studied the population inversion of binary Lennard–Jones mixtures confined in nanopores.<sup>17</sup> They show that the interaction strength, size ratio of the components, confinement size, and thermodynamic state have an effect on the population inversion. However, many studies were restricted to the symmetric nonadditive hard-sphere and binary Lennard–Jones mixtures. Actually, the population inversion of the asymmetric nonadditive fluid mixtures affects on the size ratio of the components and confinement effects by the nonadditive walls.<sup>8–10</sup> The purpose of this paper is to elucidate the nature of the population inversion in nanopores using the density

Received: July 12, 2011

Revised: February 16, 2012

Published: February 21, 2012



functional theory of symmetric and asymmetric nonadditive mixtures. Through this work we show that the population inversion is the typical shift first-order fluid–fluid demixing transition due to the confinement effect in nanopores. The population inversion can only be observed in nanopores with finite widths. For this we will introduce the nonadditive penetrable mixtures<sup>19–22</sup> with a bounded potential, where the fluid–fluid demixing transition may occur. We study the equilibrium properties of nonadditive penetrable mixtures confined in two hard flat walls. Justification of the penetrable model lies in the fact that it features all characteristic properties of bounded potential while having a relatively simple form.<sup>19–22</sup> The penetrable model can be seen as a limiting case of the generalized exponential model<sup>23</sup> with a finite interaction. In the limit  $T \rightarrow 0$ , the penetrable model clearly reduces to the hard-sphere model, where  $T$  is the temperature. The study of such a model is not of purely academic interest.<sup>19</sup> Notable examples include, for instance, the micelle in a solvent as well as the star polymer solution where two particles can interpenetrate to a substantially smaller distance. On the other hand, the bounded potential, although simple, has been served as a model in order to find the adequacy of different integral equation theories in statistical mechanics and gives rise to a rather exotic phase behavior occurring in soft matter such as the re-entrant melting and clustering of particles in a certain structural site.<sup>18,24</sup>

The remainder of the paper is organized as follows. In section II, we will describe the molecular model and propose the density functional theory (DFT), which is based on the mean-field approximation (MFA), for studying the bulk phase diagram and interfacial properties of nonadditive penetrable mixtures confined in the hard slit pores. As investigated in this work, the success of the MFA for the purely repulsive system at high density provides a satisfactory basis for applications of such model systems in nanopores.<sup>23,25,26</sup> In section III, we calculate the bulk phase diagram and particle density distributions of confined nonadditive penetrable mixtures. We show that the density jump/drop, i.e., the population inversion, in nanopores is caused by the extra repulsion between unlike species and affected by the mole fraction of species, size ratio of the components, and nonadditive walls. We also show that the population inversions are restricted at the particular values of the mole fraction, size ratio of the components, and nonadditivity. Finally, we summarize and draw our conclusions in section IV.

## II. MOLECULAR MODEL AND THEORY

We consider a nonadditive penetrable mixture consisting of species 1 and 2 in which the molecules interact via the bounded potential

$$\begin{aligned}\phi_{ij}(r) &= \varepsilon_{ij} \quad 0 \leq r \leq \sigma_{ij} \\ &= 0 \quad r > \sigma_{ij}\end{aligned}\quad (1)$$

where  $\sigma_{ij}$  ( $i, j = 1, 2$ ) is the diameter of a particle and  $\varepsilon_{ij}$  the strength of the potential energy between particles when they penetrate. The Lorentz–Berthelot combining rule for the cross interaction  $\varepsilon_{12}$  has been assumed as  $\varepsilon_{12} = (\varepsilon_{11}\varepsilon_{22})^{1/2}$ . When  $\varepsilon_{ij} = \infty$ , which is equivalent to the low-temperature limit, the pair potential reduces to the hard-sphere potential. The cross-species diameter is  $\sigma_{12} = (1/2)(\sigma_{11} + \sigma_{22})(1 + \Delta)$ , where  $\Delta$  is the nonadditivity parameter. If  $\Delta < 0$ , the nonadditivity is considered negative and positive if  $\Delta > 0$ . For positive

nonadditivity, this model is expected to separate into one rich in 1 species and the other rich in 2 species phases due to the extra repulsion between unlike species.

Following the DFT,<sup>27,28</sup> the grand potential,  $\Omega[\rho_1, \rho_2]$ , which is a functional of the one-body particle density  $\{\rho_i(\vec{r})\}$ ,  $i = 1, 2$ , is defined by the Legendre transform of the intrinsic (Helmholtz) free energy  $F[\rho_1, \rho_2]$  such that

$$\Omega[\rho_1, \rho_2] = F[\rho_1, \rho_2] + \sum_{i=1}^2 \int d\vec{r} \rho_i(\vec{r}) [u_i^{\text{ext}}(\vec{r}) - \mu_i] \quad (2)$$

where  $u_i^{\text{ext}}(\vec{r})$  is the external potential of species  $i$  and  $\mu_i$  the chemical potential. In the DFT, the equilibrium particle density distribution  $\rho_i(\vec{r})$  is determined by the minimum of the grand potential  $\Omega[\rho_1, \rho_2]$  satisfying the Euler–Lagrange relation

$$\mu_i = \frac{\delta F[\rho_1, \rho_2]}{\delta \rho_i(\vec{r})} + u_i^{\text{ext}}(\vec{r}), \quad i = 1, 2 \quad (3)$$

The intrinsic free energy functional  $F[\rho_1, \rho_2]$  is the sum of the ideal gas term  $F_{\text{id}}[\rho_1, \rho_2]$  and the excess contribution  $F_{\text{ex}}[\rho_1, \rho_2]$  originating from the particle interactions. The ideal gas contribution  $F_{\text{id}}[\rho_1, \rho_2]$  is known exactly as

$$\beta F_{\text{id}}[\rho_1, \rho_2] = \sum_{i=1}^2 \int d\vec{r} \rho_i(\vec{r}) [\ln \rho_i(\vec{r}) - 1] \quad (4)$$

where  $\beta = 1/k_B T$  and  $k_B$  is the Boltzmann constant. It should be mentioned that the thermal de Broglie wavelength  $\Lambda_i$  for species  $i$  has been suppressed. For the excess free energy we employ the MFA

$$F_{\text{ex}}[\rho_1, \rho_2] = \frac{1}{2} \sum_{i,j=1}^2 \int d\vec{r} \rho_i(\vec{r}) \int d\vec{s} \rho_j(\vec{s}) \phi_{ij}(|\vec{r} - \vec{s}|) \quad (5)$$

which provides an accurate result for systems interacting through the ultrasoft potential at high density.<sup>23,25,26</sup> Kim et al.<sup>26</sup> have recently shown that at high temperature the MFA for the penetrable mixture compares with the computer simulation very well even for the higher densities. Then, the equilibrium particle density distribution  $\rho_i(\vec{r})$  becomes, after some manipulations

$$\begin{aligned}\ln \left[ \frac{\rho_i(\vec{r})}{\rho_i} \right] \\ = -\beta u_i^{\text{ext}}(\vec{r}) + \sum_{j=1}^2 \int d\vec{s} \beta \phi_{ij}(\vec{r} - \vec{s}) [\rho_j(\vec{s}) - \rho_j], \\ i = 1, 2\end{aligned}\quad (6)$$

where  $\rho_i$  denotes the bulk density of species  $i$ . Given the external potential  $\beta u_i^{\text{ext}}(\vec{r})$  and boundary condition we can calculate the equilibrium particle density distribution  $\rho_i(\vec{r})$  of a nonadditive penetrable mixture confined in nanopores.

## III. RESULTS AND DISCUSSION

**A. Symmetric Nonadditive Penetrable Mixtures in Nanopores.** We consider a symmetric nonadditive penetrable mixture with the same diameter  $\sigma_{11} = \sigma_{22}$  and strength  $\varepsilon_{11} = \varepsilon_{22}$ .

In this case, the cross-species diameter becomes  $\sigma_{12} = \sigma(1 + \Delta)$ , where we set  $\sigma \equiv \sigma_{11} = \sigma_{22}$ . The strength becomes  $\varepsilon \equiv \varepsilon_{ij}$ . The bulk phase diagrams of the nonadditive penetrable mixtures can be calculated through the compressibility route (spinodal) and virial route (binodal). The coexisting equilibrium densities, i.e., binodal curve, can be obtained from the condition of the equality of pressure  $\beta P$  and chemical potentials  $\beta\mu_i$  of both species in the two demixed phases

$$\beta P = -\Phi + \sum_{i=1}^2 \rho_i \frac{\partial \Phi}{\partial \rho_i} \quad \text{and} \quad \beta\mu_i = \frac{\partial \Phi}{\partial \rho_i} \quad (7)$$

where  $\Phi \equiv \Phi(\rho_T, x_1)$  is the total free energy per volume,  $\rho_T = \rho_1 + \rho_2$  the total bulk density, and  $x_i = \rho_i/\rho_T$  the mole fraction of species  $i$ . In the MFA, the total free energy simply becomes, from eqs 4 and 5

$$\begin{aligned} \Phi(\rho_T, x_1) = & \rho_T [\ln \rho_T - 1 + x_1 \ln x_1 + (1 - x_1) \\ & \times \ln(1 - x_1)] + \frac{1}{2} \rho_T^2 [x_1^2 \beta \phi_{11}(k=0) \\ & + 2x_1(1 - x_1) \beta \phi_{12}(k=0) \\ & + (1 - x_1)^2 \beta \phi_{22}(k=0)] \end{aligned} \quad (8)$$

where  $\phi_{ij}(k=0)$  is the value of the Fourier transform of the potential at  $k=0$ . The spinodal curve delimiting the region of the stability against fluctuation, where the compressibility and bulk correlation length diverges, has been calculated from

$$\left( \frac{\partial^2 \Phi}{\partial \rho_1^2} \right) \left( \frac{\partial^2 \Phi}{\partial \rho_2^2} \right) - \left( \frac{\partial^2 \Phi}{\partial \rho_1 \partial \rho_2} \right)^2 = 0 \quad (9)$$

The critical points located on the spinodals and the binodals are evaluated<sup>29</sup>

$$s^3 \frac{\partial^3 \Phi}{\partial \rho_1^3} + 3s^2 \frac{\partial^3 \Phi}{\partial \rho_1^2 \partial \rho_2} + 3s \frac{\partial^3 \Phi}{\partial \rho_1 \partial \rho_2^2} + \frac{\partial^3 \Phi}{\partial \rho_2^3} = 0 \quad (10)$$

with  $s = -(\partial^2 \Phi / \partial \rho_1 \partial \rho_2) / (\partial^2 \Phi / \partial \rho_1^2)$ .

The phase diagrams are illustrated in Figure 1 for different temperature  $T^*$  and nonadditivity parameter  $\Delta$ , where  $T^* = k_B T / \varepsilon$  is the reduced temperature. This mixture exhibits the two-phase region which is bounded by the binodal curve. Above the bulk two-phase separation curves the fluid separates into two phases: one rich in 1 species and the other rich in 2 species. The binodal curve meets the spinodal one at the critical points ( $x_1 = x_2 = 1/2$ ) due to symmetry, where the demixing happens. Upon decreasing the temperature  $T^*$  and increasing the nonadditivity  $\Delta$ , the coexistence interval slowly broadens, whereas the critical density at  $x_1 = 1/2$  relatively decreases because of the extra repulsion between unlike species: the strong repulsion between unlike species favors demixing. This result implies that the fluid–fluid demixing transitions of a bulk fluid are strongly affected by the height of the repulsive barrier  $\varepsilon$  and the extra repulsion between unlike species  $\Delta$ .

We consider the symmetric nonadditive penetrable mixtures confined between two hard walls with the slit width  $H$ . In this case, the fluid–pore interaction between particles of species  $i$

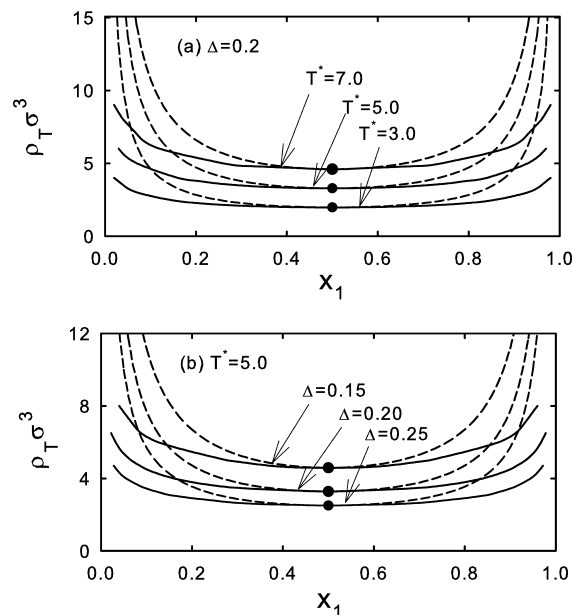


**Figure 1.** (a) Bulk phase diagrams of the nonadditive penetrable mixtures. Two-phase regions are bounded by the binodal (solid lines), which meets the spinodal (dotted lines) at the critical points (solid circles): (a)  $\Delta = 0.2$  and (b)  $T^* = 5.0$ .

with the pore walls,  $u_i^{\text{ext}}(z)$ , is a hard-sphere type in the  $z$  direction perpendicular to the slit pore wall

$$\begin{aligned} u_i^{\text{ext}}(z) &= 0 \quad \sigma/2 \leq z \leq H - \sigma/2 \\ &= \infty \quad \text{otherwise} \end{aligned} \quad (11)$$

For the numerical calculations, the diameter  $\sigma$  was taken as the unit length. The standard Picard iteration technique and trapezoidal method with  $\Delta\sigma = 0.01$  have been used to calculate the particle density distribution  $\rho_i(z)\sigma^3$  and grand potential  $\beta\Omega[\rho_1(z), \rho_2(z)]$  of the confined nonadditive penetrable mixtures.

The calculated adsorption and desorption curves of species  $i$  are displayed in Figure 2a as a function of the total bulk density  $\rho_T \sigma^3$ , where  $H = 5\sigma$ ,  $\Delta = 0.2$ , and  $x_1 = 0.1$ . The mean density  $\bar{\rho}_i$  of species  $i$  inside nanopores has been calculated

$$\bar{\rho}_i = 1(H - \sigma) \int_{\sigma/2}^{H-\sigma/2} dz \rho_i(z), \quad i = 1, 2 \quad (12)$$

where the mean density  $\bar{\rho}_i$  is related to the excess adsorption  $\Gamma_i$  defined as  $\Gamma_i = \int_{\sigma/2}^{H-\sigma/2} dz [\rho_i(z) - \rho_i] = (H - \sigma)(\bar{\rho}_i - \rho_i)$ . At low  $\rho_T \sigma^3$ , species 2 is preferably adsorbed because  $x_2 > x_1$ . However, at the particular density  $\rho_T \sigma^3 \approx 4.935$ , the mean density of species 2,  $\bar{\rho}_2 \sigma^3$ , has a sudden drop and decreases with increasing total bulk density, whereas the mean density  $\bar{\rho}_1 \sigma^3$  of species 1 shows the opposite density behavior and a sudden jump at  $\rho_T \sigma^3 \approx 4.935$ : the bulk density of species 1,  $\rho_1 \sigma^3$ , is lower than the mean density of  $\bar{\rho}_1 \sigma^3$  for all  $\rho_T \sigma^3$ , whereas  $\rho_2 \sigma^3$  is higher than  $\bar{\rho}_2 \sigma^3$ . Also of interest is the desorption branch. The desorption branch can be obtained from eq 6 by decreasing  $\rho_T \sigma^3$  from above  $\rho_T \sigma^3 \approx 4.935$ . In this case, the mean density of species 1 (or 2) has a sudden jump (or drop) at  $\rho_T \sigma^3 \approx 4.315$ . These two solutions imply the presence of metastable states within the interval  $4.315 < \rho_T \sigma^3 < 4.935$ . The point at which the curve crosses itself has two solutions with distinct morphologies. Thus, we can consider that this hysteresis loop comes from the added energy cost for particles of species 1 and 2 to mix and the

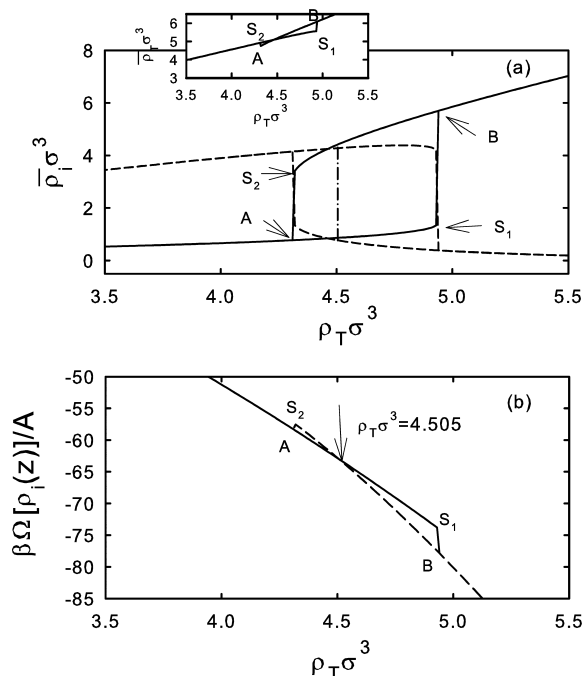


**Figure 2.** (a) Adsorption and desorption curves of the nonadditive penetrable mixtures in nanopores, where  $T^* = 5.0$ ,  $\Delta = 0.2$ ,  $x_1 = 0.1$ , and  $H = 5\sigma$ . Solid and dashed lines denote  $\bar{\rho}_1\sigma^3$  and  $\bar{\rho}_2\sigma^3$ , respectively. The dash-dotted line indicates the transition point. Insert shows  $\bar{\rho}_i\sigma^3$ . (b) Grand potential  $\beta\Omega[\rho_1(z), \rho_2(z)]/A$ . Intersection point at  $\rho_T\sigma^3 \approx 4.505$  indicates the transition point.

tendency of the fluid to adsorb at the wall. The locus of the population inversion can be determined by analyzing the dependence of the grand potential in a pore as a function of the chemical potential at  $x_1$ :<sup>30</sup>  $\beta P = -\beta\Omega[\rho_1(z), \rho_2(z)]/[A(H - \sigma)]$ , where  $P$  is the pressure and  $A$  the area of a planar interface. The grand potential of a fluid in the pore,  $\beta\Omega[\rho_1(z), \rho_2(z)]/A$ , becomes, from eqs 2, 4, and 5

$$\begin{aligned} & \frac{\beta\Omega[\rho_1(z), \rho_2(z)]}{A} \\ &= \sum_{i=1}^2 \int dz \rho_i(z) [\ln \rho_i(z) - 1] \\ &+ \frac{1}{2} \sum_{i,j=1}^2 \int dz \rho_i(z) \int dz' \rho_j(z') \beta u_{ij}(|z - z'|) \\ &+ \sum_{i=1}^2 \int dz \rho_i(z) [\beta u_i^{\text{ext}}(z) - \beta \mu_i] \end{aligned} \quad (13)$$

The cross on the curve of the grand potential versus the chemical potential represents the locus of the transition point. Notice here that we plotted the grand potential as a function of the bulk density  $\rho_T\sigma^3$  corresponding to the chemical potential for comparison with Figure 2a. This point is illustrated in Figure 2b, where the intersection point at  $\rho_T\sigma^3 = 4.505$  indicates the population inversion point. The vertical dash-dotted line in Figure 2a locates the average densities  $\bar{\rho}_i\sigma^3$  in pore at which the population inversion between two species occurs. The turnover points  $S_1$  and  $S_2$  correspond to the limit of the adsorption and desorption. At these points, the grand potentials inside the pores vary discontinuously.

Figure 3 gives the particle density distribution  $\rho_i(z)\sigma^3$  of the confined nonadditive penetrable mixtures with  $\Delta = 0.2$  just

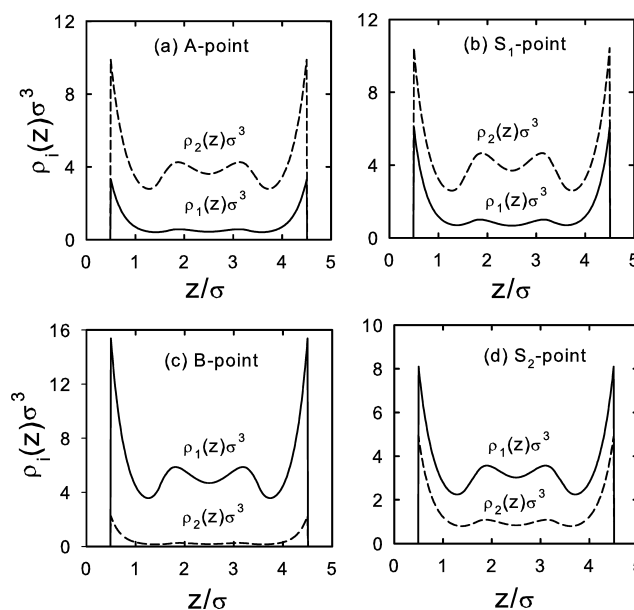


**Figure 3.** Particle density distribution of the nonadditive penetrable mixtures in nanopores, where  $T^* = 5.0$ ,  $\Delta = 0.2$ ,  $x_1 = 0.1$ , and  $H = 5\sigma$ :  $\rho_T\sigma^3 =$  (a) 4.31, (b) 4.93, (c) 4.94, and (d) 4.32.

before and after the condensation phenomenon (the points A, B,  $S_1$ , and  $S_2$  in Figure 2). At the A point, the system adopts structures in which species 2 has more population at walls due to the tendency of the molecules to maximize the system's entropy and energy effect; the energy effects also increase the tendency of molecules to locate at the walls compared to other regions. At the B point ( $\rho_T\sigma^3 = 4.94$ ), the particle density distributions  $\rho_i(z)\sigma^3$  dramatically change compared with  $\rho_1(z)\sigma^3$  at the  $S_1$  point. They show the strong adsorption with the high contact density at the wall and the layered structure. The density jump means that species 1 is replacing species 2 from the nanopores. However, there is no layering transition (or the thin–thick film transition) in nanopores. This result explains that there is no onset of the wetting transition.<sup>7,9,10</sup> This phenomenon, the population inversion, can be explained as follows: the extra added energy cost by increasing the total bulk density influences the density development of species  $i$  at the walls and in the middle of the pores even though the bulk density ratio  $\rho_1/\rho_2 = x_1/(1-x_1)$  is a constant. Species 1 starts to absorb more strongly at the walls, replacing species 2 from the walls by the competition between the packing effect and the configurational entropic effect; the increasing density differences near the wall results in a higher excluded volume and energy effect near the slit wall, and eventually the higher excluded volume and energy effect cause a strong particle density development in nanopores. In this case, the correlation length increases and results in stronger tendency to the population inversion. The strong particle density development of the deficient species 1 near the wall prompts a population inversion in nanopores, which illustrates the rich species 2 being reduced and deficient species 1 being increased. Here, one interesting thing is the population inversion of nonadditive penetrable mixtures in a single-slit wall, where  $H \rightarrow \infty$ . For the single-slit wall, the contact density  $\rho_i(z = \sigma/2)\sigma^3$  at the wall exactly satisfies the pressure sum rule



such as  $\beta p = \sum_{i=1,2} \beta p_i = \sum_{i=1,2} \rho_i(z = \sigma/2)$ , where  $\beta p_i$  is the partial pressure of species  $i$ . The particle densities in the region far from the slit wall are exactly the same as the bulk densities of species  $i$ . This means that for the single-slit wall the pressure changes continuously with increasing total bulk density and the population inversion is not observed. Thus, we can conclude that the population inversion can only be observed in finite pores.<sup>7,9,10</sup>

The calculated mean density,  $\bar{\rho}_1 \sigma^3$ , inside the slit pore is displayed in Figure 4a as a function of temperature, where

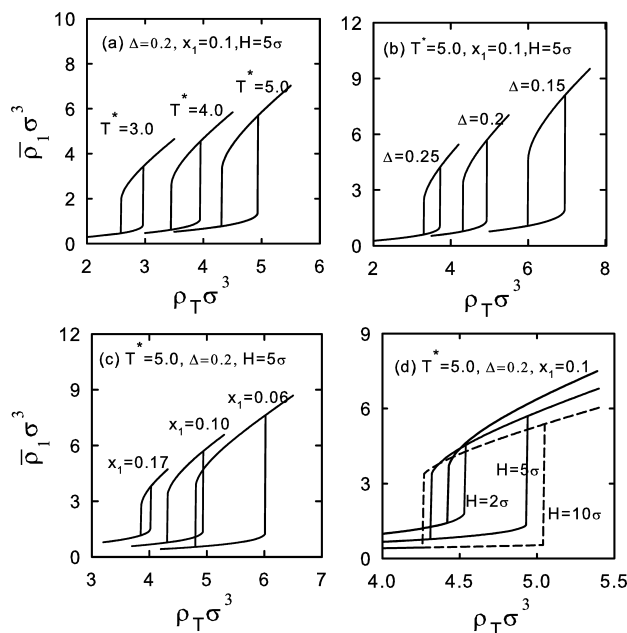


**Figure 4.** Adsorption and desorption curves for species 1: (a)  $\Delta = 0.2$ ,  $x_1 = 0.1$ , and  $H = 5\sigma$ , (b)  $T^* = 5.0$ ,  $x_1 = 0.1$ , and  $H = 5\sigma$ , (c)  $T^* = 5.0$ ,  $\Delta = 0.2$ , and  $H = 5\sigma$ , and (d)  $T^* = 5.0$ ,  $\Delta = 0.2$ , and  $x_1 = 0.1$ .

$\Delta = 0.2$ ,  $x_1 = 0.1$ , and  $H = 5\sigma$ . The wide hysteresis loop implies the temperature effect by an extra repulsion between unlike species. At a high temperature  $T^*$ , the added energy cost for particles of species 1 and 2 to mix is smaller than that of the low temperature. The tendency of the fluid to adsorb at the wall is relatively reduced. Thus, the adsorption and desorption curves are observed at higher density. The adsorption and desorption curves of species 1 as a function of the nonadditivity parameter  $\Delta$  are presented in Figure 4b, where  $T^* = 5.0$ ,  $x_1 = 0.1$ , and  $H = 5\sigma$ . Adsorption and desorption curves are observed at lower density with increasing nonadditivity. The hysteresis loop becomes narrower with increasing nonadditivity. The hysteresis loop disappears at a particular value, i.e.,  $\Delta \approx 0.30$  for  $H = 5\sigma$ , even though we did not display these results in Figure 4b. In this case, the population inversion disappears. This means that the large extra repulsion of unlike species induces the narrow hysteresis loop: the increase of nonadditivity (or the decrease of temperature) restricts the correlation lengths in nanopores and results in a weaker tendency to population inversion. Finally, the hysteresis loop disappears at upper particular nonadditivity (or at a lower particular temperature): the average density of species 1 continuously increases with increasing total bulk density, whereas the average density of species 2 decreases. Figure 4c and 4d presents the effects of mole fraction and slit width for the adsorption and desorption branches. The results suggest that the confinement effect plays an important role in

determining the composition of fluids in nanopores. As expected from Figure 3, the hysteresis loop becomes narrower with increasing mole fraction  $x_1$ , while the hysteresis loop becomes wider with increasing pore width  $H$ . Finally, it disappears at a particular value.

In Figure 5 we displayed the confinement effect by the external potential, where we have taken the nonadditive wall for species 2 such as

$$u_2^{\text{ext}}(z) = 0 \quad \sigma/2 + \Delta \leq z \leq H - (\sigma/2 + \Delta) \\ = \infty \quad \text{otherwise} \quad (14)$$

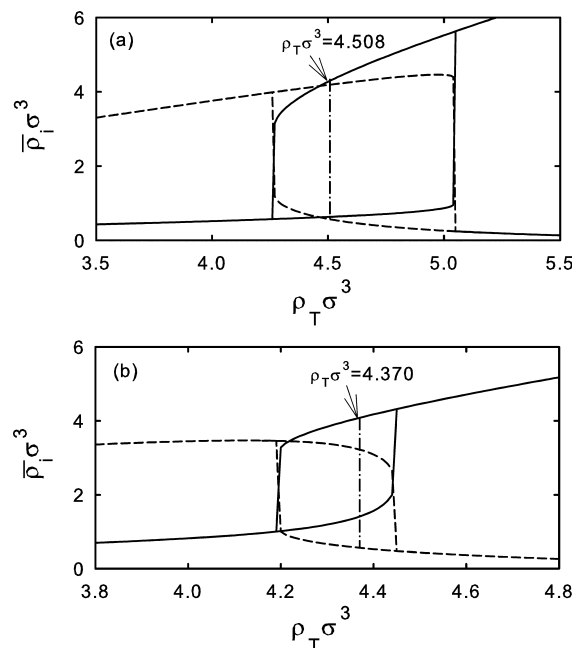


**Figure 5.** Adsorption and desorption curves ( $x_1 = 0.1$ ,  $\Delta = 0.2$ ,  $T^* = 5.0$ , and  $H = 10\sigma$ ). Solid and dashed lines denote  $\bar{\rho}_1 \sigma^3$  and  $\bar{\rho}_2 \sigma^3$ , respectively. The dash-dotted line denotes the population inversion line determined from the grand potential: (a) additive wall ( $u_2^{\text{ext}} = \sigma/2$ ) and (b) nonadditive wall ( $u_2^{\text{ext}}(z) = \sigma/2 + \Delta$ ).

In this case, one expects species 2 to adsorb more strongly at the wall. As can be seen from Figure 5, the nonadditive wall affects the population inversion of a nonadditive penetrable mixture in nanopores. The nonadditive wall for species 2, i.e., confinement effect, leads to the population inversion in lower density compared with that of the additive wall: the transition density  $\rho_T \sigma^3 \approx 4.370$  for the nonadditive wall is lower than  $\rho_T \sigma^3 \approx 4.508$  for the additive one. Figure 6 shows the population inversion lines for  $H = 5\sigma$  and  $10\sigma$  together with the binodal curves of the bulk system, where  $T^* = 5.0$  and  $\Delta = 0.2$ . Recall that the population inversion line does not coincide with the population inversion in the adsorption and desorption curves. The population inversion line for the additive walls lies at slightly lower density compared with the coexistence curves of the bulk system. It is extended for the higher values of  $x_1$  with increasing width of slit pores and finally terminated at the particular total density  $\rho_T \sigma^3$  and mole fraction  $x_1$ : for the additive walls ( $H = 5\sigma$ ), the population inversion terminates at  $x_1 \approx 0.24$  ( $\rho_T \sigma^3 \approx 3.600$ ), whereas  $x_1 \approx 0.094$  ( $\rho_T \sigma^3 \approx 4.233$ ) for the nonadditive walls. This result is very different from the fluid–fluid demixing transition in nanopores. The coexistence curve in nanopores is shifted toward a higher density compared

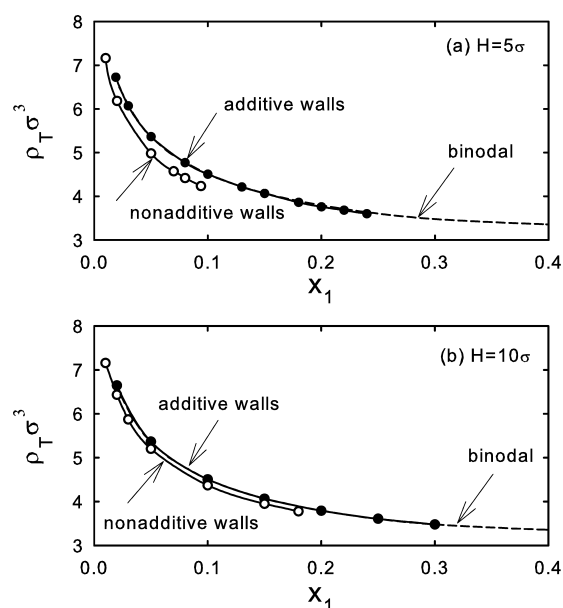


**Figure 6.** Population inversion line ( $T^* = 5.0$  and  $\Delta = 0.2$ ):  $H =$  (a)  $5\sigma$  and (b)  $10\sigma$ . Dotted line denotes the binodal curve of the bulk system.

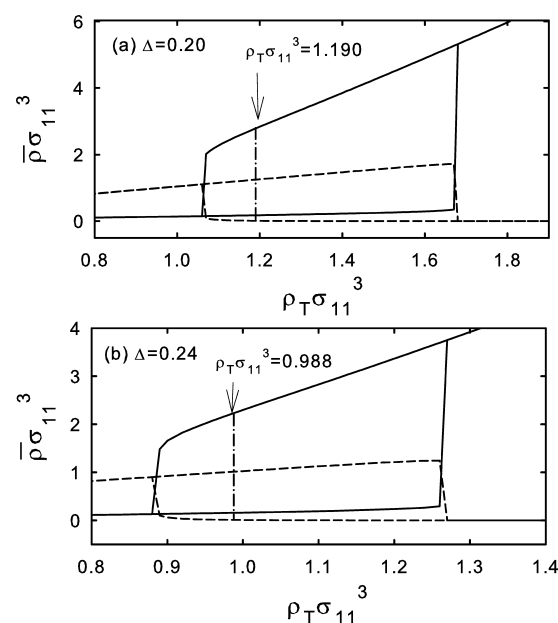
with that of the bulk system.<sup>3,4,15</sup> The reason is that close to the critical point the correlation length increases; thus, in one direction perpendicular to the walls the correlations are restricted due to the confinement that results in a weaker tendency to population inversion. Figure 6 illustrates that the population inversion occurs at a lower density with increasing confinement for species 2. This means that the higher density of species 2 at the wall due to the nonadditive wall prompts the population inversion in lower bulk density compared with that of the additive wall. These similarities support the observation that (i) the population inversion diagram for the nonadditivity hard-sphere mixtures is shifted toward a higher fluid density with decreasing width of slit pores<sup>3,4,15</sup> and (ii) the population inversion line of the nonadditive hard-spheres mixtures is close to the bulk fluid coexistence line but two phenomena are different.<sup>11</sup> Thus, we can conclude that the population inversion is not the typical shift of the fluid–fluid demixing transition due to the confinement effects but one of many phenomena in nanopores.

**B. Asymmetric Nonadditive Penetrable Mixtures in Nanopores.** To study the size ratio of the component and confinement effects by the nonadditive walls, we consider the asymmetric nonadditive penetrable mixtures confined between two hard walls with slit width  $H$ . In this case, the fluid–pore interaction between particles of species  $i$  with the pore walls,  $u_i^{\text{ext}}(z)$ , is a hard-sphere type in the  $z$  direction perpendicular to the slit pore wall

$$u_i^{\text{ext}}(z) = 0 \quad \sigma_{ii}/2 + d_i \leq z \leq H - (\sigma_{ii}/2 + d_i) \\ = \infty \quad \text{otherwise} \quad (15)$$

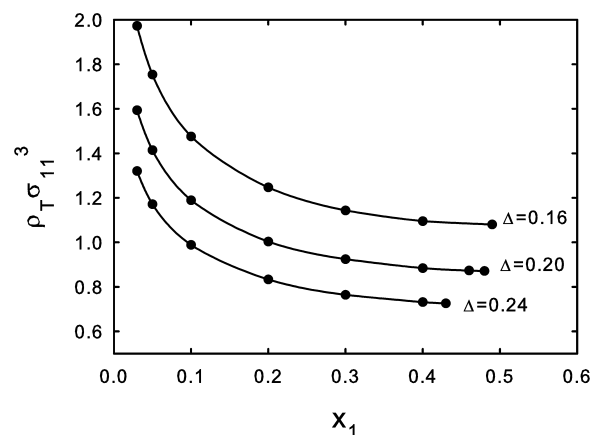
where  $d_i = (1/2)(\sigma_{11} + \sigma_{22})\Delta$ .<sup>10</sup> For the additive wall it becomes  $d_i = 0$ . For the numerical calculations, the diameter  $\sigma_{11}$  has been taken as the unit length. The standard Picard iteration technique and trapezoidal method with  $\Delta\sigma_{11} = 0.01$  have been used.

Figure 7 shows the mean density of the asymmetric nonadditive penetrable mixtures with the size ratio  $\sigma_{22}/\sigma_{11} = 2$  inside the additive walls, where  $H = 10\sigma_{11}$ ,  $T^* = 5.0$ , and  $x_1 = 0.1$ .



**Figure 7.** Adsorption and desorption curves of the asymmetric nonadditive penetrable mixtures ( $H = 10\sigma_{11}$ ,  $\sigma_{22}/\sigma_{11} = 2$ ,  $T^* = 5.0$ , and  $x_1 = 0.1$ ). Solid and dashed lines denote  $\bar{\rho}_1\sigma^3$  and  $\bar{\rho}_2\sigma^3$ , respectively. Dash-dotted lines denote the population inversion lines:  $\Delta =$  (a)  $0.2$  and (b)  $0.24$ .

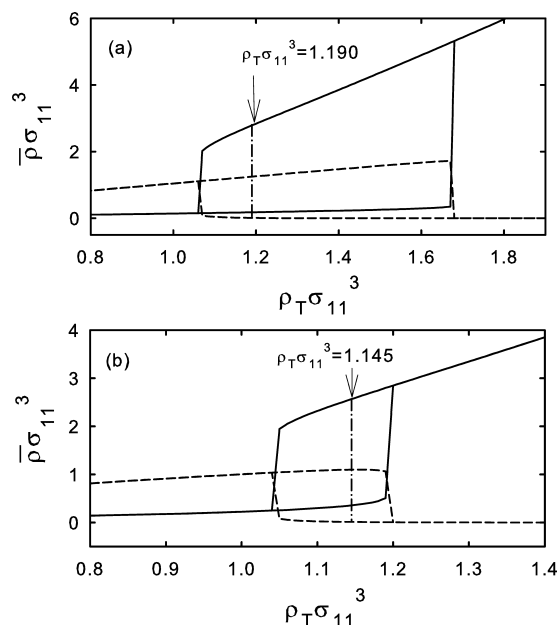
The dash-dotted lines in Figure 7a and 7b denote the population inversion lines, where the true thermodynamic equilibrium occurs only when the adsorption and desorption grand potentials come across. The increase of the nonadditivity  $\Delta$  leads to the population inversion in lower density: the transition density  $\rho_T\sigma_{11}^3 \approx 0.988$  for  $\Delta = 0.24$  is lower than  $\rho_T\sigma_{11}^3 \approx 1.190$  for  $\Delta = 0.2$ . The adsorption and desorption curves show the wide hysteresis loops for the low nonadditivity. Here, one interesting thing is the population inversion of the asymmetric nonadditive penetrable mixtures in a single-slit wall. As can be expected from a symmetric system, there is no the population inversion for the asymmetric system. However, the prewetting transition (or thin–thick film transition) is expected because of the asymmetric nonadditivity.<sup>7,10,23</sup> The population inversion lines for three different nonadditivity inside the additive wall ( $d_1 = d_2 = 0$ ) have been displayed in Figure 8,



**Figure 8.** Population inversion lines of the asymmetric nonadditive penetrable mixtures inside the additive walls ( $H = 10\sigma_{11}$ ,  $\sigma_{22}/\sigma_{11} = 2$ , and  $T^* = 5.0$ ).

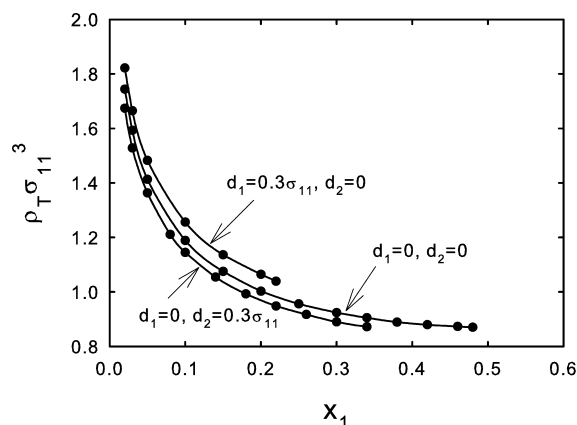
where  $H = 10\sigma_{11}$ ,  $\sigma_{22}/\sigma_{11} = 2.0$ , and  $T^* = 5.0$ . The population inversion is observed at lower density with increasing the nonadditivity. In this case, the wide hysteresis loops are expected for the low nonadditivity as can be expected from Figure 7. We can check that the large size ratio of components also leads to the population inversion in lower density compared with that of the symmetric nonadditive penetrable mixtures. Once again, this result implies that the increase of nonadditivity restricts the correlation lengths in nanopores and results in a weaker tendency to the population inversion.

Figure 9 shows the adsorption and desorption curves for the asymmetric nonadditive penetrable mixtures with the size ratio



**Figure 9.** Adsorption and desorption curves of the asymmetric nonadditive penetrable mixtures inside the nonadditive walls ( $H = 10\sigma_{11}$ ,  $\sigma_{22}/\sigma_{11} = 2$ ,  $T^* = 5.0$ ,  $\Delta = 0.2$ , and  $x_1 = 0.1$ ). Solid and dashed lines denote  $\bar{\rho}_1\sigma_1^3$  and  $\bar{\rho}_2\sigma_2^3$ , respectively. Dash-dotted line denotes the population inversion line: (a)  $d_1 = d_2 = 0$  and (b)  $d_1 = 0$ ,  $d_2 = 0.3\sigma_{11}$ .

$\sigma_{22}/\sigma_{11} = 2$  inside the additive and nonadditive walls, where  $H = 10\sigma_{11}$ ,  $T^* = 5.0$ ,  $\Delta = 0.2$ , and  $x_1 = 0.1$ . The nonadditive wall for species 2 leads to the population inversion in lower density and the narrow hysteresis loop compared with that of the additive wall: the transition density  $\rho_T\sigma_{11}^3 \simeq 1.190$  for the additive wall is higher than  $\rho_T\sigma_{11}^3 \simeq 1.145$  for the nonadditive one. The reason is that the repulsion for species 2 due to the nonadditive walls develops the strong density profiles near the walls and prompts the population inversion at the lower density compared with that of the additive wall. Once again, this means that the nonadditive wall has the effect which increases the nonadditivity between unlike species in the additive walls. The population inversion lines for three different nonadditive walls have been depicted in Figure 10, where  $\sigma_{22}/\sigma_{11} = 2.0$ ,  $H = 10\sigma_{11}$ ,  $T^* = 5.0$ , and  $\Delta = 0.2$ . The nonadditive wall for species 2 leads to the population inversion in lower density and terminates in higher mole fraction  $x_1$  compared with that of the nonadditive wall for species 1. These results indicate that the nonadditive wall for species 2 develops the strong density profiles of species 2 near the wall. Thus, the population inversion occurs at a lower density compared with that of the nonadditive walls for species 1: the higher the confinement for



**Figure 10.** Population inversion lines of the asymmetric nonadditive penetrable mixtures inside the nonadditive walls ( $H = 10\sigma_{11}$ ,  $\sigma_{22}/\sigma_{11} = 2$ ,  $T^* = 5.0$ , and  $\Delta = 0.2$ ).

species 2 the lower the density at which the population inversion occurs. Thus, we can conclude that the nonadditive wall strongly affects the population inversion: for the single additive wall there is no preferential adsorption at the wall and hence no layering transition.<sup>7,9,23</sup>

#### IV. CONCLUDING REMARKS

We employed the mean-field approximation (MFA), which provides an accurate result for systems interacting through the ultrasoft potential at a high density, for studying the population inversion of nonadditive penetrable mixtures in nanopores. The calculated result shows that the population inversion is strongly affected by the extra repulsion between unlike species, the mole fraction of species, the nanopore width, and the nonadditive walls. The wide hysteresis loops are observed for the wide slit pore, the low mole fraction, and the low nonadditivity. The population inversion lines are extended for the higher values of mole fraction with increasing width of slit pores. Finally, the density jump curve meets the density drop one and terminates at the critical values. The population inversion is the shift first-order fluid–fluid demixing transition due to the confinement effect. The population inversion can only be observed in the finite pores. Furthermore, the size ratio of the components and nonadditive wall strongly affect the population inversion of the model fluids in nanopores. The nonadditive wall for the big particles leads to the population inversion in lower density. The population inversion line is terminated at a higher mole fraction  $x_1$  compared with that of the nonadditive wall for the small particles.

Here, one interesting question is whether the population inversion can be observed for the fluid system which exhibit the fluid–fluid demixing transition of the bulk system or not. For this we investigated the population inversion of the Widom–Rowlinson mixtures.<sup>31</sup> However, there is no the population inversion in nanopores. This result suggests that the model fluids exhibiting the fluid–fluid demixing transition of the bulk systems do not guarantee the population inversion in nanopores. On the other hand, we can expect the population inversion to occur in a large variety of systems where the demixing transition of the bulk system is relevant. Bryk<sup>34</sup> recently studied the surface phase transition close to the corresponding bulk phase transition of the colloid–polymer mixture, where the polymers are modeled as the freely jointed hard-sphere chain. Recall that there is a fluid–fluid demixing

transition only when the ratio of the colloid diameter to the monomer diameter is large enough.<sup>32</sup> The similar surface-induced phase transition was recently studied by McGarrity et al.,<sup>33</sup> where the transition is governed by the polymer chain length and colloid density. This system does not sit near a corresponding bulk phase transition and the ratio of the colloid diameter ( $\sigma_c$ ) to the monomer diameter ( $\sigma_p$ ) is not large enough, i.e.,  $\sigma_c/\sigma_p = 2.0$ . However, they did not report the population inversion effect for this mixture. Also of interest is the population inversion of binary Lennard–Jones mixtures confined in nanopores.<sup>22</sup> The interaction strength, size ratio of the components, confinement size, and thermodynamic state have an effect on the population inversion. It is very interesting to test the population inversion for the confined colloid–polymer mixtures and generalized exponential model,<sup>8</sup> which exhibit the fluid–fluid demixing transition of the bulk systems.<sup>34,35</sup>

## AUTHOR INFORMATION

### Corresponding Author

\*Phone: +82-54-820-5444. Fax: +82-54-823-1628. E-mail: sckim@andong.ac.kr.

### Present Address

†Department of Physics, Kyungpook National University, Taegu, 702-701, Korea.

### Notes

The authors declare no competing financial interest.

## ACKNOWLEDGMENTS

This research was supported by the Basic Science Research Program through the National Research Foundation of Korea (NRF) funded by the Ministry of Education, Science and Technology (Grant No. (2011-0021133) and the HANARO Center of Korea Advanced Energy Research Institute (KAERI) through the National Nuclear Technology Program.

## REFERENCES

- (1) Gelb, L. D.; Gubbins, K. E.; Radhakrishnan, R.; Sliwinski-Bartkowiak, M. *Rep. Prog. Phys.* **1999**, *62*, 1573.
- (2) Jagannathan, K.; Yethiraj, A. *J. Chem. Phys.* **2003**, *118*, 7907.
- (3) Duda, Y.; Vakarin, E.; Alejandre, J. *J. Colloid Interface Sci.* **2003**, *258*, 10.
- (4) Gózdź, W. T. *J. Chem. Phys.* **2005**, *122*, 074505.
- (5) Brader, J. M.; Vink, R. L. C. *J. Phys.: Condens. Matter* **2007**, *19*, 036101.
- (6) (a) Schmidt, M. *Phys. Rev. E* **2007**, *76*, 031202. (b) Santos, A. *Phys. Rev. E* **2007**, *76*, 062201.
- (7) Hopkins, P.; Archer, A. J.; Evans, R. *J. Chem. Phys.* **2006**, *129*, 214709.
- (8) Overduin, S. D.; Likos, C. N. *Europhys. Lett.* **2009**, *85*, 26003.
- (9) Camargo, M.; Likos, C. N. *Mol. Phys.* **2011**, *109*, 1121.
- (10) Hopkins, P.; Schmidt, M. *Phys. Rev. E* **2011**, *83*, 050602(R).
- (11) Jiménez-Ángeles, F.; Duda, Y.; Odriozola, G.; Lozada-Cassou, M. *J. Phys. Chem. C* **2008**, *112*, 18028.
- (12) Kim, S.-C.; Suh, S.-H.; Seong, B.-S. *J. Korean Phys. Soc.* **2009**, *54*, 660.
- (13) Ayadim, A.; Amokrane, A. *J. Phys. Chem. B* **2010**, *114*, 16824.
- (14) Brunet, C.; Malherbe, J. G.; Amokrane, S. *J. Chem. Phys.* **2009**, *131*, 221103.
- (15) Brunet, C.; Malherbe, J. G.; Amokrane, S. *Phys. Rev. E* **2010**, *82*, 021504.
- (16) Taghizadeh, A.; Keshavarzi, E. *J. Phys. Chem. B* **2011**, *115*, 3551.
- (17) Bucior, K.; Patrykiewicz, A.; Pizio, O.; Sokolowski, A. *J. Colloid Interface Sci.* **2003**, *259*, 209.
- (18) van Teeffelen, S.; Moreno, A. J.; Likos, C. N. *Soft Matter* **2009**, *5*, 1024.
- (19) Marquest, C.; Witten, T. A. *J. Phys. (Fr.)* **1989**, *50*, 1267.
- (20) Schmidt, M. *J. Phys.: Condens. Matter* **1999**, *11*, 10163.
- (21) (a) Malijevský, A.; Yuste, S. B.; Santos, A. *Phys. Rev. E* **2007**, *76*, 021504. (b) Santos, A.; Malijevský, A. *Phys. Rev. E* **2007**, *76*, 021201.
- (22) Khanpour, M.; Hashim, R. *J. Chem. Phys.* **2008**, *129*, 164508.
- (23) Likos, C. N.; Mladek, B.; Gottwald, D.; Kahl, G. *J. Chem. Phys.* **2007**, *126*, 224502.
- (24) Likos, C. N.; Lang, A.; Watzlawek, M.; Löwen, H. *Phys. Rev. E* **2001**, *63*, 031206.
- (25) Archer, A. J.; Likos, C. N.; Evans, R. *J. Phys.: Condens. Matter* **2004**, *16*, L297.
- (26) Kim, S.-C.; Seong, B.-S.; Suh, S.-H. *J. Chem. Phys.* **2009**, *131*, 134701.
- (27) Hansen, J.-P.; McDonald, I. R. *Theory of Simple Liquids*, 3rd ed.; Academic Press: London, 2006.
- (28) Evans, R. *Adv. Phys.* **1979**, *28*, 143.
- (29) Rowlinson, J. S. *Liquids and Liquid Mixtures*; Butterworths: London, 1959.
- (30) (a) Schlijper, A. G.; Telo da Gama, M. M.; Ferreira, P. G. *J. Chem. Phys.* **1993**, *98*, 1534. (b) Vishnyakov, A.; Piotrovskaya, E. M.; Brodskaya, E. N.; Votyakov, E. V.; Tovbin, Y. K. *Langmuir* **2001**, *17*, 4451. (c) Patrykiewicz, A.; Pizio, O.; Sokolowski, S.; Sokolowska, Z. *Phys. Rev. E* **2004**, *69*, 061605. (d) Bryk, P.; Bucior, K.; Sokolowski, S.; Zukociński, G. *J. Phys. Chem. B* **2005**, *109*, 2977. (e) Peng, B.; Yu, Y.-X. *J. Phys. Chem. B* **2008**, *112*, 15407.
- (31) Widom, B.; Rowlinson, J. S. *J. Chem. Phys.* **1969**, *52*, 1670.
- (32) Paricaud, P.; Varga, S.; Jackson, G. *J. Chem. Phys.* **2003**, *118*, 8525.
- (33) McGarrity, E. S.; Frischknecht, A. L.; Frink, L. J. D.; Mackay, M. E. *Phys. Rev. Lett.* **2007**, *99*, 238302.
- (34) Bryk, P. *J. Chem. Phys.* **2006**, *125*, 204709.
- (35) Schmidt, M.; Fortini, A.; Dijkstra, D. M. *J. Phys.: Condens. Matter* **2003**, *15*, S3411.